Isomorphous Substitution of Mn(II) into Aluminophosphate Zeotypes: A Combined High-Field ENDOR and DFT Study

D. Arieli,*,† A. Delabie,‡ D. E. W. Vaughan,§ K. G. Strohmaier,‖ and D. Goldfarb*,†

Department of Chemical Physics, Weizmann Institute of Science, Rehovot, Israel, 76100,
Department of Chemistry, University of Leuven, Celestijnenlaan 200F, B-3001 Heverlee-Leuven, Belgium,
Materials Research Laboratory, Pennsylvania State University, University Park, Pennsylvania 16802, and
Exxon Research and Engineering Company, Route 22 East, Annandale, New Jersey 08801

The incorporation of low levels of Mn(II) (Mn/Al∼0.001) into five aluminophosphate zeotypes was studied by high-field echo-detected EPR, and by ^{31}P and ^{1}H electron−nuclear double resonance (ENDOR) spectroscopies. The zeotype structures investigated−SOD, AEL, AFI, SBS, and SBT−cover a variety of channel morphologies, and span a range of framework densities. The highly resolved EPR spectra could distinguish between two types of Mn with different ^{55}Mn hyperfine couplings in structures containing more than one T site. Mims and Davies ^{31}P ENDOR spectra, recorded at a field set to one of the $|-^{1}/_{2}, m_l\rangle \rightarrow |+^{1}/_{2}, m_l\rangle$ ^{55}Mn hyperfine components consist of a symmetric doublet, with a splitting in the range of 5−8 MHz. The large open structures showed smaller couplings than the denser morphologies. A similar ^{31}P hyperfine was also detected for Fe(III) incorporated into aluminophosphate zeotype with the SOD structure. Variations in the ^{1}H ENDOR spectra of the various Mn(II) substituted zeotypes, particularly in the relative intensity of the ^{1}H matrix line, were detected as well. These ENDOR results indicate a common mechanism of framework substitution in which Mn(II) and Fe(III) are replacing Al (or Mg). Moreover, the spectra serve as a probe for the differences in the local environment and bonding topology of these substituted framework sites. A qualitative interpretation of the ^{31}P ENDOR data is provided, based on relevant crystallographic information, and the ^{1}H ENDOR signals are partially attributed to the interactions with the templates occluded in the zeotype cages. To further relate the isotropic ^{31}P hyperfine couplings to structural properties, DFT methods were employed for cluster model optimizations and hyperfine coupling constants calculations. Geometry optimizations of substituted rings, derived from the SOD and AEL framework structures, indicate considerable distortions of the coordination environment of framework Mn as compared to Al. A systematic study of the hyperfine interactions of a series of model structures containing tetrahedral and octahedral Mn(II) show that both Mn−O bond lengths and Mn−O−P bond angles contribute significantly to the variation in the isotropic and anisotropic ^{31}P hyperfine coupling.

Introduction

Aluminophosphate molecular sieves (AlPO's)[1,2] form a family of synthetic zeotypes, containing more than two dozens of three-dimensional framework structures.[3] The majority of the AlPO's are microporous materials, synthesized hydrothermally at 100−250 °C from reaction mixtures containing structure-directing organic templates. Their first discovery in 1982 by Wilson et al.[1] has triggered the synthesis of various microporous materials based on structural and compositional modifications such as silicoaluminophosphates[4] and metal-substituted aluminophosphates (MAPO's).[5−7] This has further led to the synthesis of large cage zeotypes with multidimensional 12-ring channels.[8]

The incorporation of transition metal ions into aluminophosphate zeotypes is of particular interest as it allows for a delicate interplay between the transition metal redox properties, the zeotype acidity/basicity, and its unique pore structure.[6,9] The standard methods for metal ion incorporation are: impregnation, ion-exchange and isomorphous substitution into framework sites.

In the last method the transition metal ion is added to the synthesis mixture. Since the comprehensive paper of Flanigen et al. in 1986,[10] many studies have been published, reporting the isomorphous substitution of transition metal ions into different framework types. These have been recently reviewed by Hartman and Kevan,[9] and by Weckhuysen et al.[11]

Determining the precise atomic architecture of catalytically active sites in MAPO's is a highly relevant discipline in the design of new catalysts, and a full panoply of spectroscopic tools is often deployed depending on the nature and valence state of the transition metal ion. Over the years, infrared, UV−vis, electron paramagnetic resonance (EPR) spectroscopies, and extended-X-ray absorption fine structure (EXAFS),[12,13] have been routinely applied for characterizing transition metal ions in MAPO's. Among these techniques EPR is best suited for characterizing systems with low levels of paramagnetic transition metal ions. Nonetheless, the EPR spectrum is often not sufficient for a detailed structural characterization, and its information content is usually limited to the identification of the paramagnetic species present in the sample, their symmetry and their distribution. In the case of polycrystalline samples, the EPR spectrum suffers from low spectral resolution due to the aniso-

---

† Department of Chemical Physics.
‡ Department of Chemistry.
§ Materials Research Laboratory.
‖ Exxon Research and Engineering Company.

TABLE 1: Elemental Analysis, Given in Relative Molar Ratios for the Zeotypes Investigated, along with a Few Synthesis Parameters

sample	template used	Al source	P/Al	Mg/Al	Mn/Al
Mn-AlPO$_4$-20	tetramethylammonium hydroxide	Catapal B	0.99		0.0014
Mn-AlPO$_4$-11	di-*n*-propylamine	Catapal B	0.98		0.0009
Mn-AlPO$_4$-5	triethylmethylammonium hydroxide	Catapal B	1.00		0.0015
Mn-UCSB-6Mg	1,7-diaminoheptane	Al isopropoxide	1.75	0.71	0.0012
Mn-UCSB-10Mg	4,7,10-trioxa-1,13-tridecane diamine	Al isopropoxide	1.86	0.84	0.0016
Fe-AlPO$_4$-20	tetramethylammonium hydroxide	Catapal B	0.95		0.0008

tropic character of the various magnetic interactions that lead to extensive inhomogeneous broadening. A better mapping of the close environment of paramagnetic metal sites is provided by the electron−nuclear-double-resonance (ENDOR)[14,15] technique, which is highly useful at high-fields, particularly for $S > \frac{1}{2}$ systems. The advantages of high-fields over conventional X-band fields stem from the large thermal polarization in combination with increased sensitivity and the reduced effect of high-order terms arising from the zero field splitting (ZFS).[16,17] ENDOR applications benefit further from the appreciably large nuclear Zeeman interaction, which helps in resolving signals of nuclei with close gyromagnetic ratios (γ), and improves the detection of low γ nuclei with small hyperfine couplings.[18]

Recently, we have presented a direct evidence for isomorphous substitution of Mn(II) for Al in AlPO$_4$-20 using W-band ($\nu_0 \approx 95$ GHz) ^{31}P ENDOR.[19] The presence of a ^{31}P coupling with an isotropic hyperfine interaction, A_{iso}(^{31}P), of ≈ 8 MHz, and the absence of such an [27]Al interaction served as a combined proof for framework substitution. This study lead to the following questions: (i) Is the hyperfine coupling framework specific? (ii) Will the hyperfine coupling of a different d^5 element such as Fe(III) be similar? (iii) What is the mechanism by which Mn(II) is incorporated into the framework? The first two issues are the subjects of the current contribution, while a separate study was devoted to the last one.[20]

The recent advances in computational chemistry have contributed significantly to the progress in characterizing transition metal incorporated zeolites.[21,22] A breakthrough in this field was the formulation of density functional theory (DFT) by Kohn and Sham,[23,24] which made it possible to calculate various magnetic properties of transition metals such as NMR chemical shifts[25] and **g**-tensors[26] in a relatively low computational cost with respect to traditional ab initio techniques. However, the number of systems to which DFT methods have been applied for calculating hyperfine interactions is still rather limited;[27−29] hence, the validity and applicability of these methods for the interpretation of experimental hyperfine couplings is far from being mature.

A major complication in applying quantum chemical methods to zeolite related problems is their infinite dimension. One way to overcome this difficulty is to adopt finite models such as clusters of atoms or ions, which can be real or hypothetical molecules. This "molecular" approach is particularly suited to tackle local phenomena,[30] such as cationic substitution sites in a modified zeolite, and it helps to understand the structure and bonding properties of transition metal incorporated molecular sieves. Such an approach has been successfully used by Pierloot and co-workers[31−33] for the calculation of d−d transitions and g-values of Co(II) and Cu(II) ions occupying cationic positions in aluminosilicate zeolites, and recently also by Carl et al.[26] in DFT calculations of g-values and hyperfine coupling constants of VO^{2+} exchanged zeolites. Cheng et al.[34,35] have applied DFT in combination with X-ray absorption spectroscopy (XANES and EXAFS) to study the structure of vanadyl(IV) and vana-

dium(V) in cluster models of AlPO$_4$-5. The calculated clusters indicated that while the substitution of either P or Al in the framework is not feasible, the parameters of optimized models representing an *extraframework* substitution site are comparable with those obtained from the in-situ X-ray absorption experiments.[34]

In this paper we have examined, using high-field EPR techniques, three Mn(II) incorporated aluminophosphate structures (Mn-AlPO$_4$-20, Mn-AlPO$_4$-5, and Mn-AlPO$_4$-11), two new frameworks composed of magnesium-aluminophosphate with large open cages[8] (Mn-UCSB-6Mg and Mn-UCSB-10Mg) and one example of Fe(III) incorporated into aluminophosphate zeotype (Fe-AlPO$_4$-20). These framework structures are schematically presented in Figure 1. The interaction with the framework elements was probed by ^{31}P ENDOR and the proximity to water and template molecules was detected by ^{1}H ENDOR experiments. In addition, DFT was employed in an attempt to perform geometry optimizations of clusters composed of four-membered and six-membered rings in which one Al(III) atom is substituted by Mn(II). DFT was further used to predict trends in the hyperfine values as a function of the distortions imposed on Mn(II) coordinated to phosphoric acid ligands. Both tetrahedral and octahedral configurations were tested in order to gain an insight into the factors affecting the [55]Mn and ^{31}P hyperfine interactions.

Experimental Section

Zeotype Synthesis. The synthesis of Mn-AlPO$_4$-20 has been described previously,[19] and a similar procedure was applied for Fe-AlPO$_4$-20. Mn-AlPO$_4$-11 and Mn-AlPO$_4$-5 were prepared using standard hydrothermal procedures described elsewhere,[7,36] and the syntheses of Mn-UCSB-6Mg and Mn-UCSB-10Mg were done according to Stucky et al.[8] All samples except Mn-AlPO$_4$-5 were introduced into standard Teflon-lined steel autoclaves that were placed in a conventional oven. The crystallization of Mn-AlPO$_4$-5 was done in a microwave oven, using a microwave autoclave, which lead to a shorter crystallization time. Details about the template used and the aluminum source in each synthesis are given in Table 1, along with the ICP-AES chemical analysis data. Manganese was introduced as manganese sulfate or manganese acetate solutions, and the iron was introduced as iron chloride. The phase purity was verified by powder X-ray diffraction (XRD) using a RIGAKU D diffractometer, and the results are shown in Figure 2. All samples were ground prior to introduction into the W-band tubes.

Pulsed-EPR Measurements. W-band pulsed experiments (94.9 GHz) were carried out on a home-built spectrometer at 5 K.[37] Field swept echo detected (FS-ED) spectra were obtained using the two-pulse echo sequence with pulses of 40 and 60 ns, and a repetition rate of 0.5 kHz. All ENDOR experiments were carried out at a field set to $g \sim 2$, which for the Mn(II) containing samples corresponds to one of the $|-\frac{1}{2}, m_I\rangle \rightarrow |+\frac{1}{2}, m_I\rangle$ [55]Mn hyperfine components. Davies-ENDOR spectra
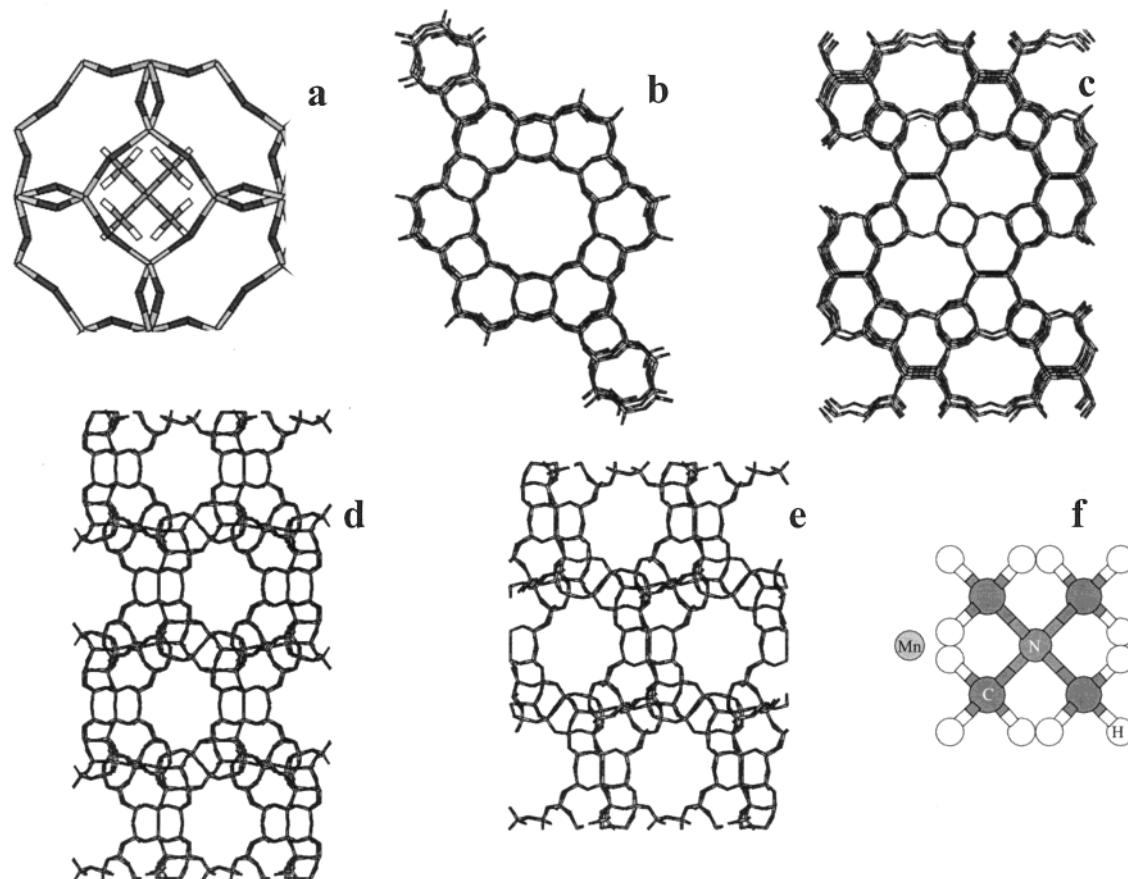
Aluminophosphate Zeotypes

J. Phys. Chem. B, Vol. 106, No. 30, 2002 **7511**

Figure 1. The structures of AlPO$_4$-20 (SOD) (a), AlPO$_4$-5 (AFI) (b), AlPO$_4$-11 (AEL) (c), UCSB-6 (SBS) (d), and UCSB-10 (SBT) (e). The SOD fragment contains also the template molecule, TMA. The structure shown in (f) includes one T site of SOD adjacent to a TMA molecule.
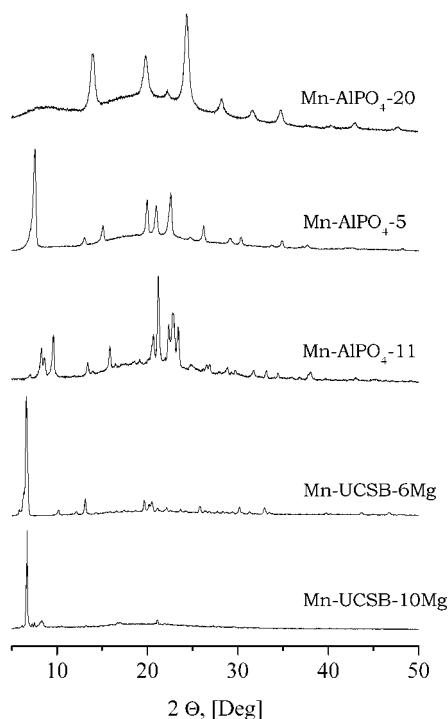

Figure 2. XRD patterns of the zeotypes investigated.

were recorded with π and $^{\pi}/_2$ MW pulse lengths of 0.2 and 0.1 μs, respectively. In the Mims-ENDOR experiments the duration of the $^{\pi}/_2$ pulses was 0.04 μs. ^{31}P Davies ENDOR experiments were measured with a typical RF pulse length (t_{RF}) of 20 μs, a

τ value of 0.3 μs, and a repetition rate of 0.5 kHz, whereas Mims-ENDOR experiments were recorded under the same conditions with a τ value of 0.7 μs. In the case of Fe-AlPO$_4$-20, t_{RF} was 10 μs and τ was set to 0.4 μs due to its shorter echo decay time. ^{1}H ENDOR experiments on the zeotype samples were carried out with $t_{RF} = 10$ μs, $\tau = 0.3$ μs and a repetition rate of 0.2 kHz. The experiment on 1 mM MnCl$_2$ in water/glycerol solution was done with $\tau = 0.45$ μs, $t_{RF} = 15$ μs, and a repetition rate of 0.1 kHz. For convenience, the frequency scale in the ENDOR spectra is given relative to the corresponding Larmor frequency.

Geometry Optimizations. Geometry optimizations were carried out by means of DFT,[23] using the Turbomole code.[38] Clusters of the form [Mn(OP(OH)$_3$)$_4$]$^{2+}$ and [Mn(OP(OH)$_3$)$_4$·2H$_2$O]$^{2+}$ were fully optimized in the gas phase using the Becke three parameters hybrid exchange functional[39] and the Lee−Yang−Parr[40] correlation functional; i.e., the combination commonly denoted as B3LYP. Basis sets from Schäfer et al.[41] were employed as follows: For Mn a triple-ζ basis set was chosen and enhanced with two polarization functions (TZVDP), while for all other atoms triple-ζ basis sets were chosen, and enhanced with one polarization function (TZP). This method, particularly the selected hybrid functional, was proven to be very successful in previous studies of transition metal systems,[42] yet its computational cost turned out to be very high for large clusters. Hence, a different (pure DFT) approach was utilized for the other optimizations; the ring-type clusters were optimized using the gradient-corrected Becke exchange[43] and Perdew correlation functional,[44] denoted BP86. Basis sets from Schäfer et al.[41] were employed. For Mn and for all O atoms linked to it a double-ζ basis set was chosen and enhanced with one polarization

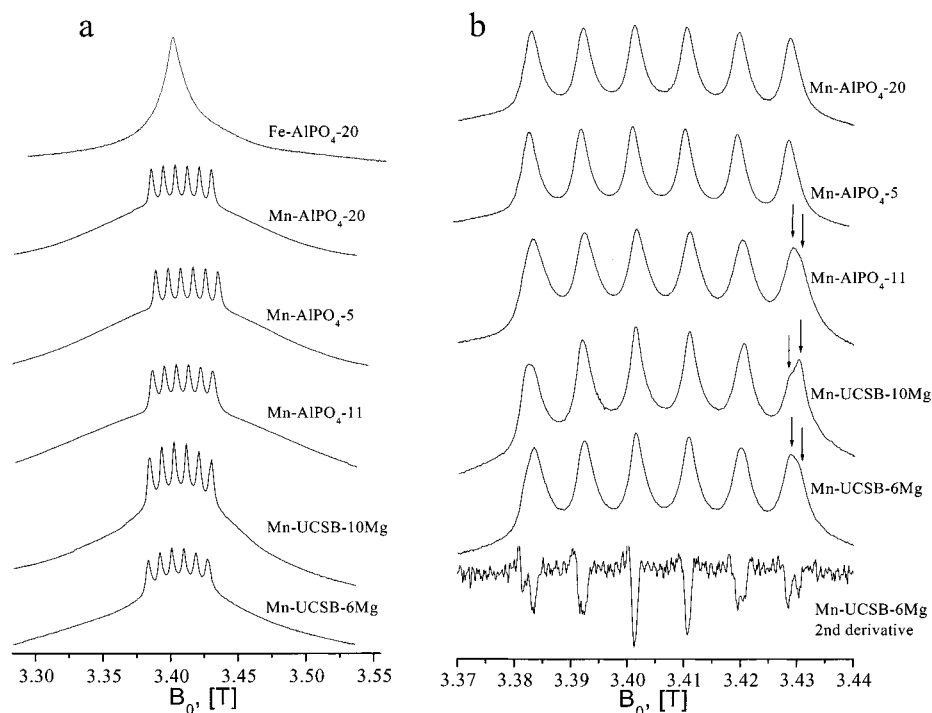**7512** *J. Phys. Chem. B, Vol. 106, No. 30, 2002*

Arieli et al.

Figure 3. FS-ED EPR spectra of the various zeotypes investigated (a) rapid scan of the full range (b) slow scan of the central range. The arrows mark the shoulders due to a second component. The bottom spectrum in (b) is the second derivative of the Mn-UCSB-6Mg spectrum.

function (DZP), while for Al, P, H, and all other oxygen atoms double-ζ basis sets were chosen (DZ). This method was previously selected by Pierloot and co-workers.[31]

The initial non substituted clusters were generated from the corresponding zeotype structures[45,46] by "cutting" the four-membered ring (4MR) or six-membered ring (6MR) from the zeotype including all oxygen atoms, and terminating all dangling bonds with hydrogen atoms.[47] These new O−H bonds were first optimized to generate the initial non substituted clusters, and then Mn(II) was substituted for Al. The negative charge created by the substitution was balanced by linking a proton to one of the internal oxygen atoms to generate clusters of the form $AlP_2MnO_{12}H_9$(4MR) and $Al_2P_3MnO_{18}H_{13}$(6MR). Two types of gas-phase optimization were then carried out: (i) Restricted optimization using internal coordinates. In this optimization the terminal OH bonds were kept fixed in their equilibrium positions while the internal frame including the Brönsted acid site (MnP_2-AlO_4H or $MnP_3Al_2O_6H$) was allowed to relax. The rationale behind this procedure, which limits the degrees of freedom during the optimization, was to obtain a "realistic" picture of the local distortions caused by the presence of Mn(II) in the otherwise rigid crystal. (ii) Unrestricted optimizations allowing a full relaxation of the cluster and employing Cartesian coordinates. The following convergence criteria were used: 10^{-6} hartree for the energy change, 10^{-3} hartree/bohr for the gradients.

Hyperfine Coupling Constants Calculations. All-electron DFT calculations of hyperfine coupling constants were done using the Amsterdam density functional (ADF)[48] code, and employing the BP86 functional. The nonrelativistic unrestricted Kohn−Sham calculations were carried out with DZP basis sets (designated as "III" for O, P, and H and "II" for Mn in the ADF package).

ENDOR Simulation. The powder ENDOR simulation was done applying EasySpin; a versatile simulation program using Matlab, developed by Schweiger and Stoll.[49] The ENDOR frequencies of an $S = 5/2$, with a small zero-field splitting ZFS

parameter coupled to n nuclei with $I = 1/2$ are given to first order by[50]

$$\nu^{ENDOR}(M_s) = \sum_{i=1}^{n} |\nu_I - M_s A_i| \qquad (1)$$

where for an axial symmetry $A_i = A_{iso_i} + T_{\perp i}(3\cos^2\theta_i - 1)$, and when the point dipole approximation applies $T_{\perp i} = [\mu_0/(4\pi h)]g_e\beta_e g_n\beta_n r^{-3}$. A_{iso_i} is the isotropic part of the hyperfine interaction, r_i is the electron−nuclear distance, θ_i is the angle between the electron−nuclear vector and the direction of the external magnetic field, and all other parameters have their usual meaning. This first-order approximation is valid for weakly coupled protons at magnetic fields used in this study.

Results and Discussion

Figure 1a−e depicts the structures of the aluminophosphate zeotypes investigated in this work: $AlPO_4$-20, $AlPO_4$-5, $AlPO_4$-11, UCSB-6Mg, and UCSB-10Mg. The XRD patterns of the as-synthesized Mn substituted materials are shown in Figure 2. The background in the patterns of Mn-$AlPO_4$-20, Mn-$AlPO_4$-5, and Mn-$AlPO_4$-11 is mainly due to the very small amount of samples used, combined with their small crystal size.

FS-ED EPR Spectra. Figure 3a shows the various FS-ED EPR spectra. They are all typical for a polycrystalline $S = 5/2$, $I = 5/2$ system at high-field. The well resolved sextet in the center of the spectrum corresponds to the $|-1/2, m_I\rangle \rightarrow |+1/2, m_I\rangle$ EPR transitions, whereas the unresolved background is due to all other transitions.[51,52] The high resolution of the sextet allows a straightforward determination of the ^{55}Mn isotropic hyperfine coupling, $A_{iso}(^{55}Mn)$, which for the samples studied is in the range of 252−274 MHz.[19,53,54] This range is typical for octahedral Mn(II),[55] although there have been reports on tetrahedral Mn(II) with similar hyperfine values.[56] Figure 3b shows only the region of the sextet which was recorded under a slower field sweep to optimize the resolution. The bottom

Aluminophosphate Zeotypes

J. Phys. Chem. B, Vol. 106, No. 30, 2002 **7513**

TABLE 2: Summary of the Parameters Describing the Topology of the Different Framework Structures and the Respective ^{55}Mn, ^{31}P and ^{1}H Hyperfine Couplings (MHz)

zeotype	code[a]	T site	ring size	density[b]	aperture[c]	$A_{iso}(^{55}Mn)$	$A_{iso}(^{31}P)$	$A_{\perp}(^{1}H)$
$AlPO_4$-20	SOD	1	4, 6	16.7	2.2	255 ± 3	8 ± 1	0.7, 1.7
$AlPO_4$-5	AFI	1	4, 6, 12	16.9	7.3	258 ± 3	8 ± 1	0.7, 1.7
$AlPO_4$-11	AEL	3	4, 6, 10	19.2	3.9×6.3	$258 \pm 3, 274 \pm 3$	7 ± 1	0.8, 2.2
UCSB-6	SBS	4	4, 6, 8, 12	12.8	7.6×7.4	$258 \pm 3, 269 \pm 3$	6 ± 1	2.2
UCSB-10	SBT	4	4, 6, 8, 12	12.8	7.6×7.4	$252 \pm 3, 271 \pm 3$	5 ± 1	

[a] International Zeolite Association codes. [b] In T sites/1000 Å³. [c] Maximal aperture dimension in Å.
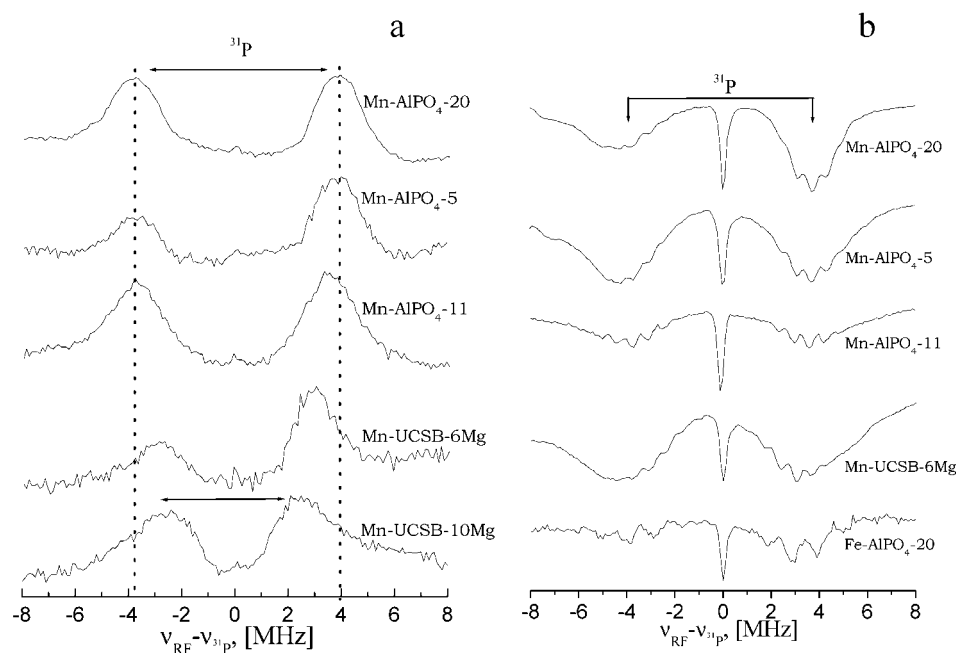
Figure 4. Selected Davies (a) and Mims (b) ^{31}P ENDOR spectra of the zeotypes investigated.

three spectra show some shoulders (marked by arrows) on both low and high field components, with Mn-UCSB-10Mg exhibiting the best resolution. This is an indication of a superposition of two sextets, due to the presence of two types of Mn(II) with slightly different $A_{iso}(^{55}Mn)$ values. The $A_{iso}(^{55}Mn)$ values extracted from Figure 3b are summarized in Table 2. In cases of two different species, second-derivative spectra were calculated in order to get the corresponding values, as shown, for example, for Mn-UCSB-6Mg (Figure 3b, bottom trace). A correlation is found between the observation of two types of Mn(II) species, and the presence of a number of T sites in the $AlPO_4$-11, UCSB-6Mg and UCSB-10Mg structures (Table 2). If all sites were populated and resolved, then one would expect three ($AlPO_4$-11) or four (UCSB-nMg) features on the six hyperfine components. We attribute the observation of only two sites to resolution limitations of the powder EPR spectrum, rather than to a preferential population of different T sites. The spectrum of Fe-$AlPO_4$-20 is a typical high-field spectrum of an $S = ^5/_2$ system with a dominant Zeeman interaction.[57]

^{31}P and ^{1}H ENDOR. The ^{31}P ENDOR measurements, recorded at a field set to one of the six ^{55}Mn hyperfine components of the central $|-^1/_2, m_I\rangle \rightarrow |+^1/_2, m_I\rangle$ transition, are presented in Figure 4. Davies ENDOR spectra are shown for all five Mn containing zeotypes, whereas Mims ENDOR spectra were recorded for most MAPO samples, and also for Fe–$AlPO_4$-20 (the Davies ENDOR of the latter could not be measured due to its fast echo decay rate). All Davies ENDOR spectra are characterized by a ^{31}P doublet, positioned symmetrically around ν_{31P} (58 MHz), the splitting of which depends on the framework type. The appearance of these ^{31}P doublets and the absence of such ^{27}Al doublets (range not shown) are

evidence for framework incorporation of Mn(II), substituting for Al or Mg in the different frameworks.[19] All Davies ENDOR spectra have an isotropic character with A_{iso} in the range of 5−8 MHz. Mims-ENDOR results further support the above interpretation, showing the typical τ dependent fine structure (Figure 4b) caused by the appearance of *blind spots*.[58] These spectra exhibit also a ^{31}P matrix line, arising from remote ^{31}P atoms (suppressed in the corresponding Davies spectra). The spectrum of Fe-$AlPO_4$-20 is similar to that of Mn-$AlPO_4$-20, although the splitting is somewhat smaller, ≈6−7 MHz (the distance between adjacent blind spots is bigger due to a smaller τ value). The asymmetry between the two hyperfine components in some of the ^{31}P ENDOR spectra (see for example the Davies ENDOR spectrum of Mn-UCSB-6Mg) is attributed to baseline imperfections, and not to the relaxation effects recently reported by Epel et al.[59]

Davies ^{1}H ENDOR spectra of all Mn containing zeotypes are shown in Figure 5, along with a reference spectrum of $MnCl_2$ in water/glycerol solution. The latter consists of three sets of singularities at ± 0.3, ± 1.2, and ± 3.5 MHz. The last two are attributed to $A_{\perp}/2$ and $A_{\parallel}/2$ of water ligands, originating from the $M_s = \pm^1/_2$ manifolds,[60] and the former one is due to distant ^{1}H atoms. None of the zeolite spectra show clear singularities at ± 3.5 MHz. Mn-$AlPO_4$-20 and Mn-$AlPO_4$-5 exhibit very similar spectra, dominated by peaks at ± 0.3 and ± 0.85 MHz, whereas in the spectrum of Mn-$AlPO_4$-11 these are shifted to ± 0.4 and ± 1.1 MHz. A different line-shape is observed for Mn-UCSB-6Mg and Mn-UCSB-10Mg. Both samples show a relatively strong peak at ν_{1H}, in Mn-UCSB-6Mg singularities at ± 1.1 MHz are also detected, whereas in Mn-UCSB-10Mg there is no clear structure.
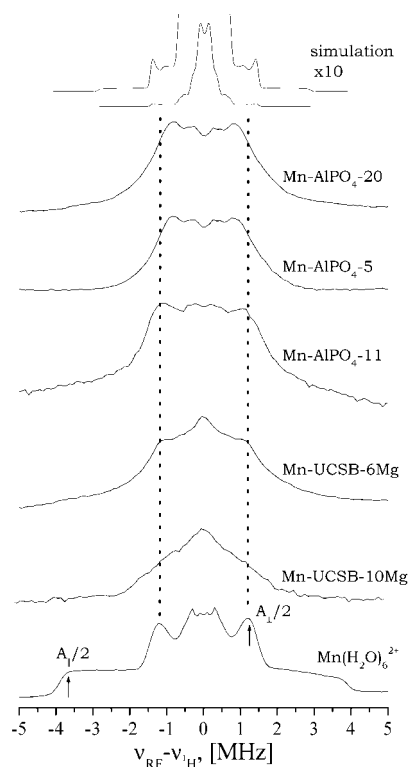
Figure 5. [1]H Davies ENDOR spectra for the zeotypes investigated. The spectrum of $[Mn \cdot 6H_2O]^{2+}$ in frozen solution is shown for reference, where the $A_{\parallel}/2$ and $A_{\perp}/2$ positions of water ligands (from $M_s = \pm12$) are indicated by arrows. Top spectrum: simulated powder pattern of the ^{1}H ENDOR calculated for the model shown in the Figure 1f. The simulation considered only the contributions from $M_s = \pm12$, and an axially symmetric hyperfine tensor was assumed for all protons. Other parameters employed: $B_0 = 3.3846$ T, and a Gaussian line shape with fwhh = 0.1 MHz.

Table 2 summarizes the main features of the ^{31}P and ^{1}H ENDOR spectra of the various MAPO's investigated, along with a few relevant parameters describing the corresponding framework type. The framework densities and aperture size are composition dependent, and in the case of UCSB-n, the parameters were taken from the analogous UCSB-6GaCo and UCSB-10Co published forms.[8] The differences in composition should be relatively small compared to the structural variation among the different framework types investigated. All samples are characterized by a single ^{31}P doublet, with relatively broad lines that mask any features due to the hyperfine anisotropy, and indicate that a distribution of $A_{iso}(^{31}P)$ values exists. The fact that the line width is only weakly dependent on the number of T sites in a given framework supports the above notion that the geometry of Mn(II) in framework sites is highly non uniform, and that a distribution of distortions is present. The main feature which distinguishes the ^{31}P ENDOR spectra from each other is the averaged $A_{iso}(^{31}P)$ value. The large open structures, characterized by lower framework densities (UCSB's), show the smallest splitting within the series of zeotype samples, whereas denser morphologies are associated with larger hyperfine values. At this stage we suggest a few explanations for the above variation: (i) differences in the Mn−O(−P) bond lengths or (ii) Mn−O−P bond angles, (iii) differences in the number and/or coordination mode of remaining water molecules within the zeotypes, and finally (iv) specific interactions with the various template molecules occluded within the zeotype cages. These four factors are independent; therefore, any combination of them is also reasonable.

The ^{1}H ENDOR results provide support for points (iii) and (iv) mentioned above. A clear distinction is found between the spectra of UCSB-nMg and the other AlPO$_4$-n structures, particularly when the intensity of the matrix line at ν^1_H is concerned. Since the singularities at ±1.2 and ±3.5 MHz, which are typical for water ligands (Figure 5, bottom trace), are practically absent from the ^{1}H ENDOR spectra of as-synthesized Mn-AlPO$_4$-20 and Mn-AlPO$_4$-5, we assign the main features in these spectra to ^{1}H nuclei of the template molecules. This is consistent with an earlier assignment of ^{1}H ESEEM data of Fe-AlPO$_4$-20, for which D$_2$O exchanged samples did not show any ^{2}H modulations[57] and with the small cage size of the AlPO$_4$-20 structure. The larger splitting detected for Mn-AlPO$_4$-11 indicates the presence of shorter Mn−H distances. These could either be a closer proximity of one of the *di-n-propylamine* protons, which is more linear than the templates used in the syntheses of Mn-AlPO$_4$-20 and Mn-AlPO$_4$-5 (see Table 1). Alternatively, it could be due to the presence of a water ligand-(s), mentioned above, which is supported by the appearance of weak tails in the corresponding ENDOR spectrum at $\approx\pm3.5$ MHz. Pentahedral and octahedral coordinations of framework Al in AlPO$_4$-n, involving one or two water ligands, have been reported for a number of as-synthesized materials.[61,62] In the case of Mn-UCSB-6Mg and Mn-UCSB-10Mg the strong matrix line in the ENDOR spectra can be attributed to an overlap of protons originating from template and water molecules remaining in the zeotype cage. The latter is supported by the relatively low framework density of these large open structures, namely, higher void space. The large size of the templates used for making these structures (see Table 2) is manifested in a broad and featureless spectrum, particularly for Mn-UCSB-10Mg.

Since a complete set of coordinates that includes all proton positions originating from the template molecule is not available, it is impossible to carry out a quantitative analysis of the ^{1}H ENDOR spectra, and one is limited to a qualitative analysis, as given above. An exception is the aluminosilicate sodalite structure, for which all the coordinates of the nitrogen and carbon atoms of the template are known[63] and can be used as a model for Mn-AlPO$_4$-20. Using the C−H bond length and bond angle of methane (1.11 Å and 107.6°, respectively), the proton positions were calculated and added to the structure, and the Mn atom was placed in an Al site. This model, shown in Figure 1f, was used to calculate all Mn−H distances, the shortest of which was found to be 3.0 Å. Using the distances of all 12 protons of a single template molecule and applying the point−dipole approximation we calculated the expected ENDOR spectrum arising from the excitation of a $|-^1/_2, m_I\rangle \rightarrow |+^1/_2, m_I\rangle$ transition, and the results are presented in the top spectrum of Figure 5. The calculations are based on eq 1, setting $A_{iso_i} = 0$. A comparison with the experimental spectrum of Mn-AlPO$_4$-20 shows that although the general width of the simulation spectrum is close to that of the experimental one (see ×10 magnification), there are disagreements in the details, namely, in the positions of the singularities and their relative intensities. The reduced intensity of signals due to small couplings (within ±0.4 MHz) in the experimental spectrum is due to the limited MW pulses selectivity,[15] which reduces the relative intensity of signals close to the Larmor frequency ($\nu_{RF} - \nu_{1_H} \sim 0$) and was not taken into account in the simulation. Moreover, the simulated spectrum is more structured and shows relatively intense singularities at $\pm(0.5-0.7)$ MHz, whereas in the experimental spectrum they appear at ±0.85 MHz. We attribute this disagreement to the fact that the simulation accounts for interactions with only one template molecule, assuming perfect

Aluminophosphate Zeotypes

J. Phys. Chem. B, Vol. 106, No. 30, 2002 **7515**

symmetry between adjacent cages containing neighboring template molecules. Allowing for a distribution in the orientation of these templates[57] will lead to an increase in the Mn$-^1$H distance distribution, and consequently to a smearing and shifting of singularities.[64] Another important source of discrepancy could be distortions created by substituting Mn(II) in an Al site, which are further discussed in Appendix A.

Calculations of Hyperfine Couplings. In this part we present an attempt to relate the experimental $A_{iso}(^{31}P)$ values to local structural parameters of the different zeotype frameworks studied. Due to their high strain, it was impossible to calculate the hyperfine interactions for the Mn-substituted rings (see Appendix A). An alternative approach was therefore undertaken, which included a systematic DFT study of the ^{31}P and ^{55}Mn hyperfine couplings for various 'perturbed' geometries of two model compounds. The first compound is tetrahedral, containing four phosphoric acid ligands, $[Mn(OP(OH)_3)_4]^{2+}$, while the second one is an octahedral cluster containing four phosphoric acids and two water ligands, namely, $[Mn(OP(OH)_3)_4 \cdot 2H_2O]^{2+}$. The latter was considered on the basis of NMR studies that reported the presence of penta- and octacoordinated framework Al in as-synthesized aluminophosphate zeotypes,[61,62] and the ENDOR results obtained for Mn-AlPO$_4$-11 that suggest the presence of one or two water ligands. Munzarova and Kaupp[27] have recently presented a detailed study in which the hyperfine coupling constants of 21 transition metal complexes were calculated using DFT methods and compared to the results of the Coupled Cluster approach.[22] They found that for the best cases, the isotropic hyperfine coupling constants could be determined to within 10$-$15%, but in other cases, particularly for superhyperfine interactions, the differences between the experimental and calculated values were even greater. On the basis of this study, we have assessed the validity of DFT in predicting trends in the hyperfine coupling constants, and showed that it is possible to obtain reproducible trends, even when the differences between the values calculated with different functionals are large.[20] The latter was also shown recently for a set of vanadyl complexes by Munzarova and Kaupp.[66]

The compounds $[Mn(OP(OH)_3)_4]^{2+}$ and $[Mn(OP(OH)_3)_4 \cdot 2H_2O]^{2+}$ were first optimized as described in the Experimental Section, and the structures obtained are shown in Figure 6a,d. These structures were used as initial models, on which the following series of modifications were imposed: out of the four similar Mn$-$O$-$P linkages, the Mn$-$O bond length and Mn$-$O$-$P bond angle of one linkage (P(1), see Figure 6a,d) were varied, while keeping the rest of the molecule frozen.[65] The Mn$-$O$-$P bond angles were selected such as to cover the range of values typical for Al$-$O$-$P angles in aluminophosphate zeotypes, while the bond lengths were in the range found for manganese oxide complexes. In what follows we shall concentrate on the isotropic hyperfine interaction, which is the dominant part and can be compared to our experimental results, and leave only little discussion for the anisotropic components.

Figure 6b,c and e,f show the variation of $A_{iso}(^{31}P)$ and $A_{iso}(^{55}Mn)$ as a function of the Mn$-$O$-$[P(1)] bond length and Mn$-$O$-$P(1) bond angle for both types of complexes. The scale in $A_{iso}(^{55}Mn)$ is different for the two complexes as tetrahedral Mn is characterized by smaller A_{iso} with respect to an octahedral configuration, in agreement with the theory.[53] Figures 6b,e show the results obtained for different Mn$-$O$-$[P(1)] bond lengths, while the Mn$-$O$-$P(1) bond angle was kept within ±1° of the optimized angle (the small variation is due to the movement of the relevant O atom). As expected, the $A_{iso}(^{31}P)$ decreases with

increasing length in both complexes, and the range of the change is similar too. The variation in $A_{iso}(^{55}Mn)$ is, however, less predicted, particularly for the octahedral complex. Figures 6c,f show the variation in $A_{iso}(^{31}P,^{55}Mn)$ as a function of the Mn$-$O$-$P(1) angle, while the Mn$-$O$-$[P(1)] bond length was fixed on the optimized length. Here, the closer the angle to 180°, the larger $A_{iso}(^{31}P)$ is. In the case of angle variation, the change in the isotropic hyperfine values of ^{55}Mn does complement the change in the hyperfine of $^{31}P(1)$, namely, a decrease in $A_{iso}(^{31}P)$ is associated with an increase in $A_{iso}(^{55}Mn)$. The 'unexpected' behavior of $A_{iso}(^{55}Mn)$ with respect to bond length variation is explained by a redistribution of the spin densities over the entire complex, such that the sum of $A_{iso}(^{55}Mn)$ and $A_{iso}(^{31}P(1))$ is no longer conserved along each series of structures. When only the angle is varied, the spin density is redistributed mainly over the ^{55}Mn and the rotating ^{31}P atom, hence the corresponding sum is practically conserved.

Considering only the hyperfine values of the optimized tetrahedral vs octahedral structures, then the larger $A_{iso}(^{31}P)$ obtained for the tetrahedral complex is associated with a smaller $|A_{iso}(^{55}Mn)|$, ($|A_{iso}(^{31}P,^{55}Mn)| = 35.7, 387$ MHz and 30.6, 431 MHz for the tetrahedral and octahedral complex, respectively) in agreement with the experimental observations. According to Table 2, all structures that show a relatively small $A_{iso}(^{31}P)$ coupling, are also characterized by two Mn components, one of which with a relatively large $A_{iso}(^{55}Mn)$. Both Mn species contribute to the ^{31}P ENDOR spectrum which lacks any resolution due to inhomogeneous broadening caused both by the ^{31}P anisotropic hyperfine interaction and the distribution in $A_{iso}(^{31}P)$. Accordingly, we attribute the smaller $A_{iso}(^{31}P)$ coupling detected for Mn-UCSB-nMg to a shift of the center of the peak caused by the presence of the species with the larger $A_{iso}(^{55}Mn)$. In all cases the calculated A_{iso} values are overestimated with respect to the experimental data presented in Table 2; in the case of ^{31}P the values are overestimated by a factor of ≈5, while for ^{55}Mn the error in A_{iso} is ≈30%. These discrepancies are attributed to spin polarization and spin contamination effects, as thoroughly discussed by Munzarova and Kaupp.[27,67] Taking these scaling factors into consideration, the 'corrected' maximal ranges for the change in $A_{iso}(^{31}P)$ and $A_{iso}(^{55}Mn)$ are ≈6 and ≈25 MHz, respectively. Both are rather close to the ranges determined experimentally and presented in Table 2.

Figure 6 clearly shows that both types of geometrical changes lead to similar variation in $A_{iso}(^{31}P)$, which suggests that it might be the combination of the two that determines the differences between different zeotypes. Table 3 summarizes the information extracted from the literature for the averaged Al$-$O bond lengths and the range of P$-$O$-$Al bond angles for the zeotypes investigated. In the case of AlPO$_4$-20 and UCSB-nMg, the published structures have different compositions than our samples,[8,45] as noted earlier in this work. With this limitation in mind, it is still possible to use Table 3 as a "rough guide", and use the Al$-$O bonds and Al$-$O$-$P angles as a reference for the Mn$-$O$-$P linkage in the substituted zeotypes. Some correlation between the averaged Al$-$O bond lengths/Al$-$O$-$P angles and the trends in the hyperfine values is found; the averaged Al$-$O bonds are longer in the UCSB structures, which can be used to explain their smaller ^{31}P hyperfine couplings. However, the effect of the angle should also be considered: the maximum Al$-$O$-$P angle in AlPO$_4$-11 and AlPO$_4$-5 is 175° and 178°, respectively, while for UCSB-6 and UCSB-10 the respective numbers are 144° and 155°, which also agrees with the trends in the hyperfine values. There are, however, experimental differences that cannot be explained by this
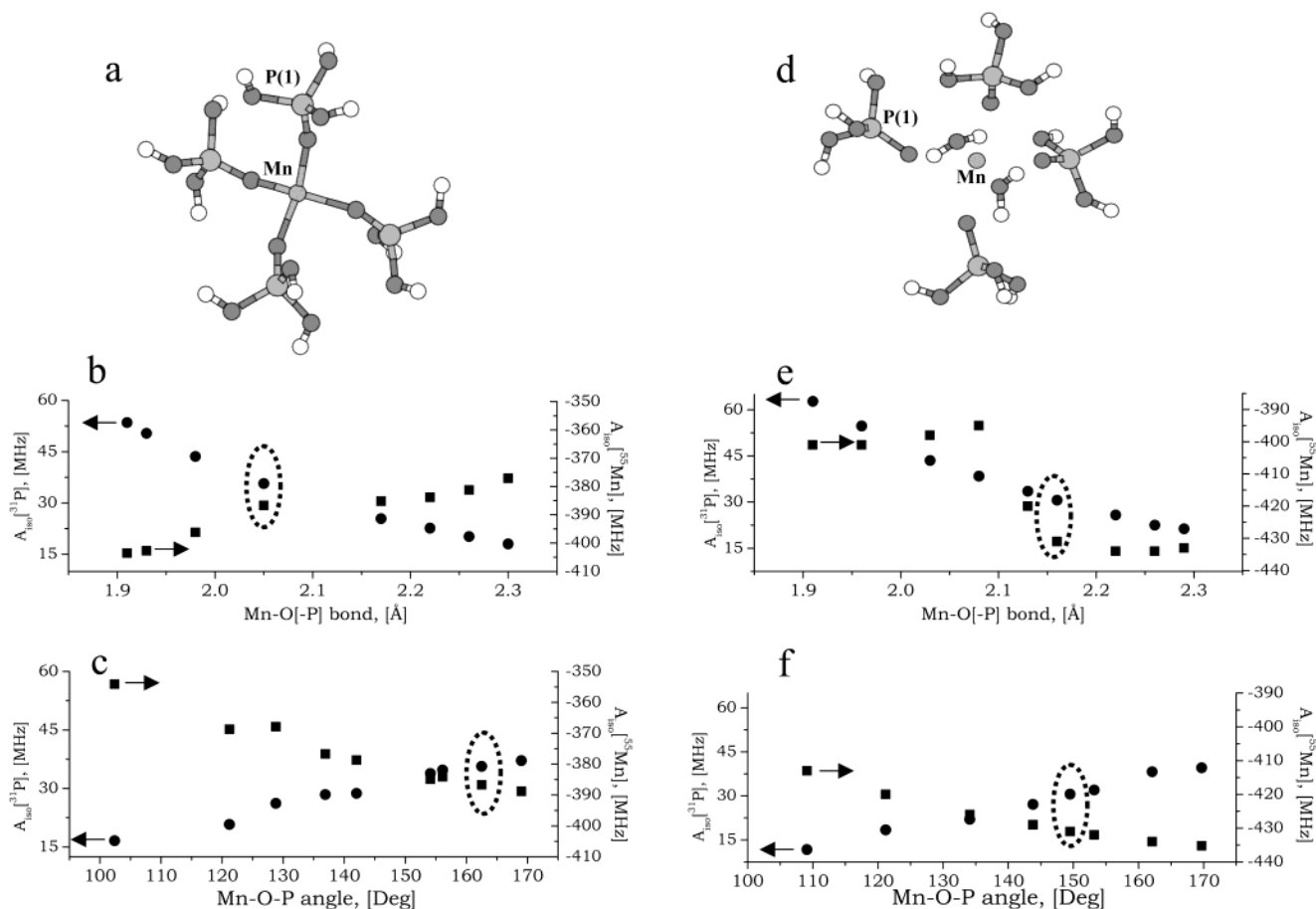
Figure 6. (a, d) The optimized structures of $[Mn(OP(OH)_3)_4]^{2+}$ (a) and $[Mn(OP(OH)_3)_4 \cdot 2H_2O]^{2+}$ (d). H atoms are in white, O atoms in black, and all other atoms are marked on the figure. The Mn−O bond lengths and Mn−O−P bond angles of the optimized structures are indicated on the graphs below with dotted circles. (b, e) The dependence of $A_{iso}(^{31}P, ^{55}Mn)$ on the Mn−O−[P(1)] bond length for the tetrahedral (b) and octahedral complexes (e). (c, f) The dependence of $A_{iso}(^{31}P, ^{55}Mn)$ on the Mn−O−P(1) bond angle for the tetrahedral (c) and octahedral complexes (f).

TABLE 3: Averaged Al−O Bond Lengths and Al−O−P Bond Angles for the Zeotypes Investigated

zeotype	Al−O, [Å]	T−O−T, [deg]
AlPO$_4$-20[45]	1.76	140
AlPO$_4$-5[69]	1.71	149−178
AlPO$_4$-11[46]	1.68	131−175
UCSB-6Mg[8]	1.85	126−144
UCSB-10Mg[8]	1.82	125−155

correlation, for example, the difference between $A_{iso}(^{31}P)$ of the two UCSB zeotypes. This implies that our model is too simplistic. Accounting for additional factors such as the O−Mn−O angle, which according to Appendix A can deviate from a tetrahedral angle, might improve the interpretation.

The variation of the largest component of the anisotropic hyperfine tensor, $T_{zz}(^{31}P)$,[68] as a function of the Mn−O−[P(1)] bond length and Mn−O−P(1) bond angle is shown for the tetrahedral complex in Figure 7. This is further compared to $2T_\perp(^{31}P)$, calculated for the same ^{31}P atom based on the point−dipole approximation[58] using the Mn−P distances of the various tetrahedral model compounds. The other two anisotropic components (T_{xx}, T_{yy}) showed that the anisotropic hyperfine interaction is generally nonaxial. There is a full correspondence between the variation of T_{zz} and $2T_\perp$ as a function of the Mn−O−[P(1)] bond length although the values of $2T_\perp$ are all smaller than T_{zz} by a factor of ~3. A similar correlation is not found for the variation with respect to the Mn−O−P(1) bond angle, which implies that T_{zz} cannot be approximated by the pure dipolar interaction model, since it has significant contributions

from direct spin densities and/or spin polarization of nonspherical ^{31}P orbitals.

The relatively large experimental $A_{iso}(^{31}P)$ values indicate substantial covalency of both Mn−O and O−P bonds. The latter was recently found by Cora and Catlow,[70] who used first-principle quantum chemical techniques to characterize the bonding properties of crystalline aluminophosphates, and compared them with silica-based zeolites. While discrete Al^{3+} ionic units were found in AlPO frameworks, the P^{5+} cations were found in larger PO_4^{3-} units, indicating that the bonding in AlPO's is ionic−molecular, rather than a continuous semi-covalent network that is present in silica and aluminosilicates. These authors also explain the relatively easy substitution of transition metal ions for Al(III) by the formation of ionic substitutional dopants, which introduce minor perturbations to the host electronic structure. The latter is, however, in contradiction with our experiments, showing a significant covalent character also for the Mn−O bonds. Calculations of the net charge on Mn employing Mulliken population analysis were done for the optimized tetrahedral complex, $[Mn(OP(OH)_3)_4]^{2+}$, at the same level of theory as the ^{55}Mn hyperfine calculations (see Experimental Section). At this level $A_{iso}(^{55}Mn)$ was overestimated by ~30%, while the calculated value for the charge is 1.15. Accounting for possible errors in this calculation, the latter is still significantly smaller than the formal charge on Mn(II), which might further indicate a covalent character of the Mn−O−(P) bond.
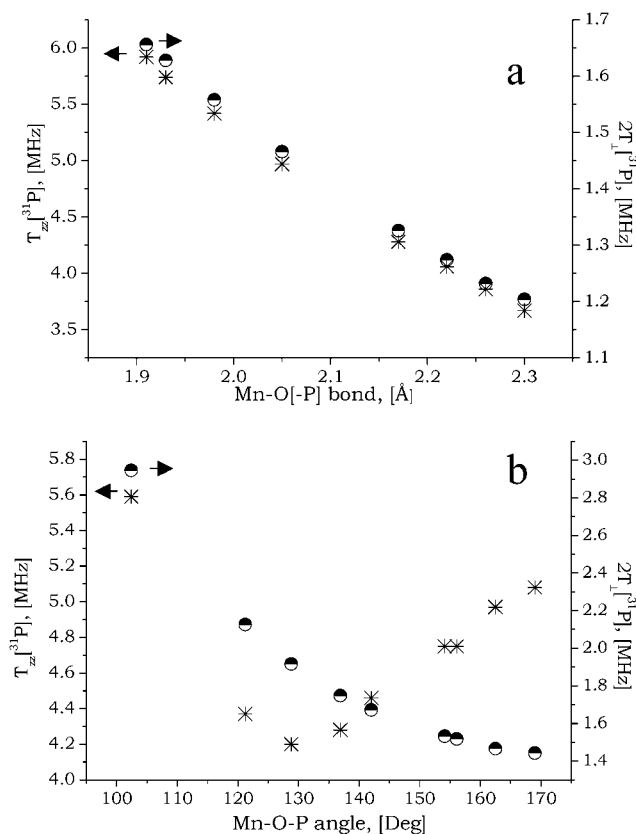
Aluminophosphate Zeotypes

J. Phys. Chem. B, Vol. 106, No. 30, 2002 **7517**

Figure 7. Plots of $T_{zz}(^{31}P)$ ($*$) and $2T_{\perp}(^{31}P)$ (semi-filled circles) for various Mn−O−[P] bond lengths (a) and Mn−O−P bond angles (b) of the complex $[Mn(OP(OH)_3)_4]^{2+}$.
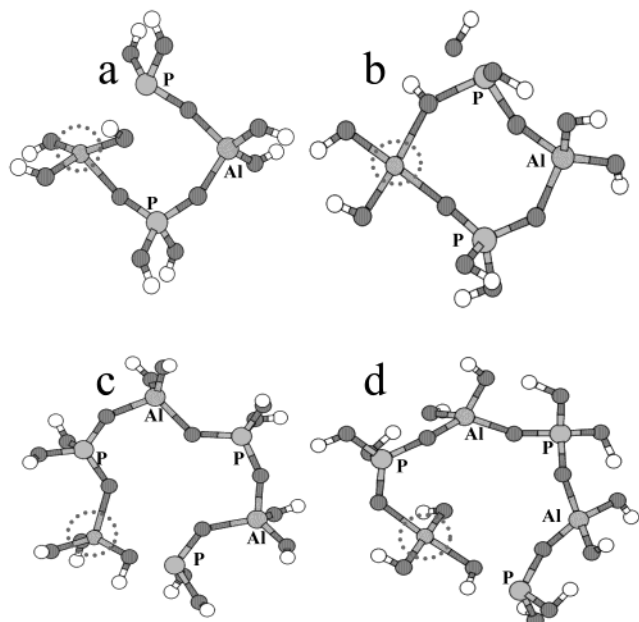

Figure 8. Optimized substituted 4MR and 6MR clusters derived from the SOD framework. The results of restricted (a, c) and unrestricted (b, d) optimizations are shown. H atoms are in white, O atoms in black, the Mn site is marked with a dotted circle, and all other atoms are indicated on the figure.

Conclusions

High-field FS-ED EPR in combination with ^{31}P and ^{1}H ENDOR provide a unique characterization of transition metal framework sites in aluminophosphate zeotypes. This was demonstrated on Mn(II) incorporated into AlPO$_4$-20, AlPO$_4$-11, AlPO$_4$-5, UCSB-6Mg, and UCSB-10Mg, as well as on Fe(III) incorporated into AlPO$_4$-20. The high resolution obtained at 95 GHz allowed to resolve two different ^{55}Mn hyperfine coupling in structures with more than one T sites. All samples are characterized by a primarily isotropic ^{31}P hyperfine coupling in the range of 5−8 MHz, where large open structures show relatively smaller couplings compared to the denser morphologies. Although a distribution in the local geometry of the Mn(II) framework sites is detected in all cases, on the average, the immediate environment of these sites vary substantially among the different frameworks.

The variations in $A_{iso}(^{31}P)$ and $A_{iso}(^{55}Mn)$ were correlated with structural properties using theoretical calculations by means of DFT. DFT calculations of $A_{iso}(^{31}P)$ for a series of model compounds containing tetrahedral/octahedral Mn(II) showed that changes in both Mn−O bond length and Mn−O−P bond angle can account for the observed differences. The ranges of hyperfine couplings in the calculations are consistent with those spanned by the experimental values.

Appendix A

The attempts to optimize representative ring type clusters for *each* of the structures investigated in this study, following a procedure similar to that described by Cheng et al.,[34] was unsuccessful. Here we present the optimized structures derived from the SOD framework, for which all possible rings were investigated. Analysis of the optimized clusters provides some insight into the strain created by framework substitution.

SOD (AlPO$_4$-20),[45] is the simplest structure containing 36 atoms in its unit cell, and the framework consists of 4MR and 6MR only. It has a highly symmetric structure, and all of its T sites are crystallographically equivalent.[3] Since the only available crystal structure is that of the analogous aluminosilicate zeolite (Si/Al = 1), the latter was taken as a model for the aluminophosphate zeotype, and all Si atoms were replaced by P atoms. Full optimization of non substituted clusters, namely, rings containing only Al and P in their T sites, showed that the differences between the reference value of the Si−O bond length and the optimized P−O bond length are very similar to the differences between the initial and optimized Al−O bond length, which justifies our model selection. These optimizations, used as a reference for the substituted rings, resulted in clusters exhibiting only small changes with respect to the initial geometries; no bond breaking occurred, and the maximum change between the reference T−O bond length and T−O-T bond angle, taken from crystallographic data, and the corresponding optimized parameters were 0.1 Å and 13°, respectively (data not shown).

Figure 8 presents the optimized Mn-substituted clusters. As opposed to the non substituted rings, these clusters did show large structural changes during the optimization. It is clear from Figure 8 that restricted optimizations failed to converge to a closed structure for both the 4MR and the 6MR (Figure 8a,c). The distances between the oxygen and disconnected phosphorus atom are 2.24 and 2.16 Å for the restricted 4MR and 6MR optimizations, respectively, and 2.17 Å for the unrestricted 6MR optimization (Figure 8d). The only case that maintained its original connectivities within the ring is the unrestricted optimization of the 4MR (Figure 8b), though one terminating OH is 2.08 Å away from its neighboring P atom (no P−O bond is, therefore, drawn for this oxygen). The geometry around Mn in this cluster is highly distorted with respect to the non substituted ring and uncommon for high-spin Mn(II); starting from a purely tetrahedral configuration found for an Al site, the optimization is directed toward a planar Mn site, with four O−Mn−O angles of ~90° and two O−Mn−O angles of ~155°. The O−Mn bond length within the internal ring is 2.0 Å.

We have also investigated possible substitution of Mn in the AEL 4MR and 6MR (the 10MR turned out to be too large for our type of calculation), which showed even more distorted clusters (data not shown). Optimizations of clusters with an additional two (or one) water ligands to form octahedral (pentahedral) Mn coordination resulted in (only) partial strain release, implying some preference for an octahedral coordination. The results obtained for the two zeotype structures indicate that the incorporation of Mn into the 4MR and 6MR of AlPO$_4$-20 and AlPO$_4$-11 creates large distortions that cannot be accommodated just by a single substituted ring. Consequently, the coordinates of additional atoms, beyond the first Mn coordination shell have to be relaxed in order to maintain the Mn atom within a framework site, which explains why restricted optimizations frequently fail to converge to a closed structure. These results are not surprising, as the preferred coordination of Mn(II) is octahedral, with an ionic radius of 0.82 Å, which is much larger than both tetrahedral and octahedral Al(III) (0.39 and 0.53 Å, respectively).[11] The incorporation of octahedrally or tetrahedrally coordinated Mn(II) is often explained by the flexibility of the aluminophosphate framework, and the presence of specific interactions with the organic template molecules.[11] This is also consistent with the low level of Mn(II) that can be incorporated into aluminophosphate frameworks (~few percents), and the fact that the stability of Mn(II) framework sites upon calcination if often low.[9,10,52] Nevertheless, a single-crystal XRD study on as-synthesized Mn-AlPO$_4$-11 with as much as Mn/Al = 0.1 showed that Mn is tetrahedrally coordinated in framework positions.[71]

To conclude this part we point out that so far most (if not all) of the successful applications of the cluster model for describing transition metal substitution sites in zeolites and zeotypes have dealt with extraframework substitution.[31−34] The results shown in this section questions the validity of the local description for Mn(II) framework sites. The application of the embedding technique, which combines quantum and molecular mechanics approaches might be a better choice for such problems. In this method the quantum mechanical description of the cluster is coupled to a classical description (with molecular modeling) of the interaction with its environment.[72,73] Successful applications of a classical approach (using the GULP software), for calculating the geometry of framework Fe(III) sites in AlPO$_4$-5 and AlPO$_4$-18, were recently recorded by Sankar et al.[74]

References and Notes

(1) Wilson, S. T.; Lock, B. M.; Messina, C. A.; Cannan, T. R.; Flanigen, E. M. *J. Am. Chem. Soc.* **1982**, *104*, 1146−1147.

(2) Szostak, R. *Molecular Sieves. Principles of Synthesis and Identification*; Van Nostrand Reinhold: New York, 1989.

(3) Treacy, M. M. J.; Higgins, J. B. *Collection of Simulated XRD Powder Patterns for Zeolites*; Elsevier Science Publishing: Amsterdam, 2001.

(4) Lock, B. M.; Messina, C. A.; Patton, R. L.; Gajek, R. T.; Cannan, T. R.; Flanigen, E. M. *J. Am. Chem. Soc.* **1984**, *106*, 6092−6093.

(5) Pyke, D. R.; Whitney, P.; Houghton, H. *Appl. Catal.* **1985**, *18*, 173−190.

(6) Flanigen, B. M.; Patton, R. L.; Wilson, S. T. In *Innovations in Zeolite Material Science*; Grobet, P. J., Mortier, W. J., Vansant, E. F., Schulz-Ekloff, G., Eds.; Studies in Surface Science and Catalysis 37; Elsevier Science Publishers: Amsterdam, 1988; p 13.

(7) Wilson, S. T.; Flanigen, E. M. In *Zeolite Synthesis*; Occelli, M. L., Robson, H. E., Eds; American Chemical Society Symposium Series; American Chemical Society: Washington, DC, 1989; p 329.

(8) Bu, X.; Feng, P.; Stucky, G. D. *Science* **1997**, *278*, 2080−2085.

(9) Hartmann, M.; Kevan, L. *Chem. Rev.* **1999**, *99*, 635−663.

(10) Flanigen, E. M.; Lock, B. M.; Patton, R. L.; Wilson, S. T. In *New Developments in Zeolite Science and Technology*; Proceedings of the 7th International Zeolite Conference, Tokyo, 1986; Murkami, Y., Lijima, A., Ward, J. W., Eds.; Kodansha Ltd.: Tokyo and Elsevier Science Publishers: Amsterdam, 1986; p 103.

(11) Weckhuysen, B. M.; Ramachandra, R. R.; Martens, J. A.; Schoonheydt, R. A. *Eur. J. Inorg. Chem.* **1999**, 565−577.

(12) Bordiga, S.; Ruzzoni, R.; Geobaldo, F.; Lamberti, C.; Giamello, E.; Zecchina, A.; Leofanti, G.; Petrini, G.; Tozzola, G.; Vlaic, G. *J. Catal.* **1996**, *158*, 486-501.

(13) Thomas, J. M. *Angew. Chem., Int. Ed.* **1999**, *38*, 3588−3628.

(14) Kurreck, H.; Kirste, B.; Lubitz, W. *Electron Nuclear Double Resonance Spectroscopy of Radicals in Solution*; VCH Publishers: New York, 1988.

(15) Gemperle, C.; Schweiger, A. *Chem. Rev.* **1991**, *91*, 1491−1505.

(16) Goldfarb, D.; Bernardo, M.; Strohmaier, K. G.; Vaughan, D. E. W.; Thomann, H.; Poluektov, O. G.; Schmidt, J. *J. Am. Chem. Soc.* **1996**, *118*, 4665−4671.

(17) Bellew, B. F.; Halkides, C. J.; Gerfen, G. J.; Griffin, R. G.; Singel, D. J. *Biochemistry* **1996**, *35*, 12186−12193.

(18) Groenen, E. J. J.; Canters, G. W.; Nar, H.; Coremans, J. W. A.; Poluektov, O. G.; Messerschmidt, A. *J. Am. Chem. Soc.* **1996**, *118*, 12141−12153.

(19) Arieli, D.; Vaughan, D. E. W.; Strohmaier, K. G.; Goldfarb, D. *J. Am. Chem. Soc.* **1999**, *121*, 6028−6032.

(20) Arieli, D.; Delabie, A.; Groothaert, M.; Pierloot, K.; Goldfarb, D. *J. Phys. Chem. B*, in press.

(21) Sauer, J. *Chem. Rev.* **1989**, *89*, 199−255.

(22) Jensen, F. *Introduction to Computational Chemistry*; John Wiley and Sons: New York, 1999.

(23) Kohn, W.; Becke, A. D.; Parr, R. G. *J. Phys. Chem.* **1996**, *100*, 12974−12980.

(24) Koch, W.; Holthausen, M. C. *A Chemist's Guide to Density Functional Theory*; Wiley-VCH: New York, 2000.

(25) Schreckenbach, G.; Ziegler, T. *Theor. Chem. Acc.* **1998**, *99*, 71−82.

(26) Carl, P. J.; Isley, S. L.; Larsen, S. C. *J. Phys. Chem. A* **2001**, *105*, 4563−4573.

(27) Munzarova, M.; Kaupp, M. *J. Phys. Chem. A* **1999**, *103*, 9966−9983.

(28) Larsen, S. C. *J. Phys. Chem. A* **2001**, *105*, 8333−8338.

(29) Neese, F. *J. Phys. Chem. A* **2001**, *105*, 4290−4299.

(30) Kramer, G. J.; de Man, A. J. M.; van Santen, R. A. *J. Am. Chem Soc.* **1995**, *113*, 6435−6441.

(31) Pierloot, K.; Delabie, A.; Ribbing, C.; Verberckmoes, A. A.; Schoonheydt, R. *J. Phys. Chem. B* **1998**, *102*, 10789−10798.

(32) Delabie, A.; Pierloot, K.; Groothaert, M. H.; Weckhuysen, B. M.; Schoonheydt, R. *Microporous Mesoporous Mater.* **2000**, *37*, 209−222.

(33) Pierloot, K.; Delabie, A.; Groothaert, M. H.; Schoonheydt, R. *Phys. Chem. Chem. Phys.* **2001**, *11*, 2174−2183.

(34) Cheng, H. Y.; Yang, E.; Lai, C. J.; Chao, K. J.; Wei, A. C.; Lee, J. F. *J. Phys. Chem. B* **2000**, *104*, 4195−4203.

(35) Cheng, H. Y.; Yang, E.; Chao, K. J.; Wei, A. C.; Liu, P. H. *J. Phys. Chem. B* **2000**, *104*, 10293−10297.

(36) Wilson, S. T.; Lok, B. M.; Flanigen, E. M. U.S. Patent 4310440, 1982.

(37) Gromov, I.; Krymov, V.; Manikandan, P.; Arieli, D.; Goldfarb, D. *J. Magn. Reson.* **1999**, *139*, 8−17.

(38) Ahlrichs, R.; Bär, M.; Häser, M.; Horn, H.; Kölmel, C. *Chem. Phys. Lett.* **1989**, *162*, 165.

(39) Becke, A. D. *J. Chem. Phys.* **1993**, *98*, 5648.

(40) Lee, C.; Yang, W.; Parr, R. G. *Phys. Rev. B* **1988**, 37.

(41) Schäfer, A.; Horn, H.; Ahlrichs, R. *J. Chem. Phys.* **1992**, *97*, 2571.

(42) Ricca, A.; Bauschlicher, C. W., Jr. *Theor. Chem. Acta* **1995**, *92*, 123.

(43) Becke, A. D. *Phys. Rev. A* **1988**, *38*, 3098.

(44) Perdew, J. P. *Phys. Rev. B* **1986**, *33*, 8822.

(45) Von Lons, J.; Schultz, H. *Acta Crystallogr.* **1967**, *23*, 434−436.

(46) Richardson, J. W.; Pluth, J. J.; Smith, J. V. *Acta Crystallogr. B* **1989**, *44*, 367−373.

(47) Aluminosilicate sodalite (Si/Al = 1) was used for AlPO$_4$-20. See further discussion later in this work.

(48) ADF 2.2. Department of Theoretical Chemistry, Vrije Universiteit: Amsterdam Baerends. See: Te Velde, G.; Bickelhaupt, F. M.; Baerends, E. J.; Fonseca Guerra, C.; Van Gisbergen, S. J. A.; Snijders, J. G.; Ziegler, T. *J. Comput. Chem.* **2001**, *22*, 931−967.

(49) Relevant documentation can be downloaded from http://www.esr.ethz.ch/.

(50) Vardi, R.; Bernardo, M.; Thomann, H.; Strohmaier, K. G.; Vaughan, D. E. W.; Goldfarb, D. *J. Magn. Reson.* **1997**, *126*, 229−241.

(51) Reed, G. H.; Markham, D. *Biological Magnetic Resonance*; Berliner, L. J., Reuben, J., Eds.; Plenum Press: 1984; Vol. 6, pp 73−142.

(52) Abragam, A.; Bleaney, B. *Electron Paramagnetic Resonance of Transition Ions*; Calderon Press: Oxford, 1970; pp 436−442.

(53) Levi, Z.; Raitsimring, A. M.; Goldfarb, D. *J. Phys. Chem.* **1991**, *95*, 7830−7838.

(54) Olender, Z.; Goldfarb, D.; Batista, J. *J. Am. Chem. Soc.* **1993**, *115*, 1106−1114.

(55) Abragam, A.; Bleaney, B. *Electron Paramagnetic Resonance of Transition Ions*; Calderon Press: Oxford, 1970; p 440.

(56) De Vos, D. E.; Weckhuysen, B. M.; Bein, T. *J. Am. Chem. Soc.* **1996**, *118*, 9615−9622.

(57) Arieli, D.; Vaughan, D. E. W.; Strohmaier, K. G.; Thomann, H.; Bernardo, M.; Goldfarb, D. *Magn. Reson. Chem.* **1999**, *37*, S43−S54.

(58) Schweiger, A.; Jeschke, G. *Principles of Pulse Electron Paramagnetic Resonance*; Oxford University Press: New York, 2001.

(59) Epel, B.; Poppl, A.; Manikandan, P.; Vega, S.; Goldfarb, D. *J. Magn. Reson.* **2001**, *148*, 388−397.

(60) Tan, X.; Bernardo, M.; Thomann, H.; Scholes, C. P. *J. Chem. Phys.* **1992**, *98*, 5147−5157.

(61) Blackwell, C. S.; Patton, R. L. *J. Phys. Chem.* **1984**, *88*, 6135−6139.

(62) Blackwell, C. S.; Patton, R. L. *J. Phys. Chem.* **1988**, *92*, 3965−3970.

(63) Baerlocher, C.; Meier, W. M. *Helv. Chim. Acta* **1969**, *52*, 1853−1860.

(64) Interactions with protons from further template molecules are negligibly small as the size of the unit cell is 9 Å, and the distance between our Mn T site and such protons is larger than 8 Å.

(65) Changing the bond length was done by moving the relevant O atom in the 111 direction. The angle was changed by locating the corresponding oxygen at the origin and rotating the O−P(OH)$_3$ fragment around any of the lab axes.

(66) Munzarova, M.; Kaupp, M. *J. Phys. Chem. B* **2001**, *105*, 12644−12652.

(67) Munzarova, M.; Kubacek, P.; Kaupp, M. *J. Am. Chem. Soc.* **2000**, *122*, 11900−11913.

(68) T_{xx} is obtained by subtraction of A_{iso} from A_{xx}, and similarly for T_{yy} and T_{zz}.

(69) Bennett, J. M.; Cohen, J. P.; Flanigen, E. M.; Pluth, J. J.; Smith, J. V. In *Intrazeolite Chemistry*; American Chemical Society: Washington, DC, 1983; p 109.

(70) Cora, F.; Catlow, R. A. *J. Phys. Chem. B* **2001**, *105*, 10278−10281.

(71) Pluth, J. J.; Smith, J. V.; Richardson, W., Jr. *J. Phys. Chem.* **1988**, *92*, 2734−2738.

(72) Rodriguez-Santiago, L.; Sierka, M.; Branchandell, V.; Sodupe, M.; Sauer, J. *J. Am. Chem. Soc.* **1998**, *120*, 1545−1551.

(73) Silhan, M.; Nachtigallova, D.; Nachitgall, P. *Phys. Chem. Chem. Phys.* **2001**, *3*, 4791−4795.

(74) Zenonos, C.; Beale, A.; Sankar, G.; Lewis, D. W.; Thomas, J. M.; Richard, C.; Catlow, A. In *Zeolites and Mesoporous Materials*; Proceedings of the 13th International Zeolite Conference, Montpellier; Galarneau, A., Di Renzo, F., Fajula, F., Védrine, J., Eds.; Elsevier Science Publishers: Amsterdam, 2001.